ARTICLE

Photoluminescence Induced by Substitutional Nitrogen in Single-Layer Tungsten Disulfide

Qingkai Qian,* Wenjing Wu, Lintao Peng, Yuanxi Wang, Anne Marie Z. Tan, Liangbo Liang, Saban M. Hus, Ke Wang, Tanushree H. Choudhury, Joan M. Redwing, Alexander A. Puretzky, David B. Geohegan, Richard G. Hennig, Xuedan Ma, and Shengxi Huang*

ACCESS | Metrics & More | Article Recommendations | Supporting Information

ABSTRACT: The electronic and optical properties of two-dimensional materials can be strongly influenced by defects, some of which can find significant implementations, such as controllable doping, prolonged valley lifetime, and single-photon emissions. In this work, we demonstrate that defects created by remote N_2 plasma exposure in single-layer WS_2 can induce a distinct low-energy photoluminescence (PL) peak at 1.59 eV, which is in sharp contrast to that caused by remote Ar plasma. This PL peak has a critical requirement on the N_2 plasma exposure dose, which is strongest for WS_2 with about 2.0% sulfur deficiencies (including substitutions and vacancies) and vanishes at 5.6% or higher sulfur deficiencies. Both experiments and first-principles calculations suggest that this 1.59 eV PL peak is caused by defects related to the sulfur substitutions by nitrogen, even though low-temperature PL measurements also reveal that not all the sulfur vacancies are remedied by the substitutional nitrogen. The distinct low-energy PL peak suggests that the substitutional nitrogen defect in single-layer WS_2 can potentially serve as an isolated artificial atom for creating single-photon emitters, and its intensity can also be used to monitor the doping concentrations of substitutional nitrogen.

KEYWORDS: WS_2, nitrogen plasma, substitution, photoluminescence, first-principles calculations
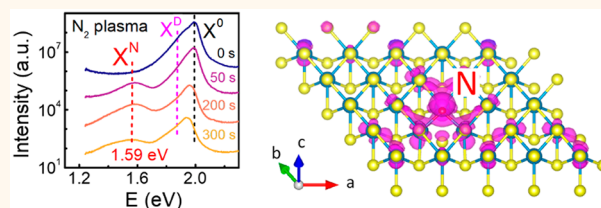
INTRODUCTION

Two-dimensional (2D) materials are widely studied for optoelectronic and quantum optical applications.[1−7] Because of their low dimensionality and reduced dielectric screening, 2D semiconductors such as WSe_2, WS_2, and MoS_2 in transition metal dichalcogenides (TMDCs) exhibit exceptionally large exciton binding energies and strong light absorptions,[1−3] based on which light-emitting diodes, solar cells, and photodetectors have already been demonstrated.[5,6] Besides, controllable valley polarization can be realized in TMDCs by circularly polarized light pumping, which allows for the manipulation of the valley degree of freedom for valleytronic device applications.[8−10] Moreover, benefiting from their flexibility for heterogeneous assembly, compatibilities of nanofabrication with Si technology, and enhanced photon extraction efficiency, 2D semiconductors are also promising solid-state platforms for single-photon emitters (SPEs),[7,11−14] which can become crucial components in the emerging quantum communications, computation, and metrology.[4,7]

The electronic and optical properties of 2D materials can be tailored by defects.[15−29] For example, controllable doping can be realized by substitutional defects in 2D materials.[15−19] W substitutions by Re can realize scalable n-type doping in

WSe_2.[19] Reproducible nitrogen doping of TMDCs through the covalent chalcogen substitutions has also been demonstrated using techniques such as remote N_2 plasma exposure, atomic nitrogen treatment, or sulfurization of metal oxynitrides.[15−17,24] Besides doping, defects in TMDCs such as the chalcogen vacancies can preserve the optical valley selectivity and prolong the valley polarization lifetime through the formation of defect-bound excitons.[25,26] Defects are also critical for SPEs based on 2D materials.[11,13,27−29] For example, crystallographic defects in h-BN are responsible for the room-temperature SPEs, even though the exact type of the corresponding defects is still under debate.[13,28] Further exploration and investigation of the promising defects in 2D materials are of fundamental importance for their device applications.[11,27−29]
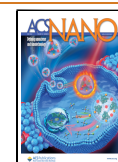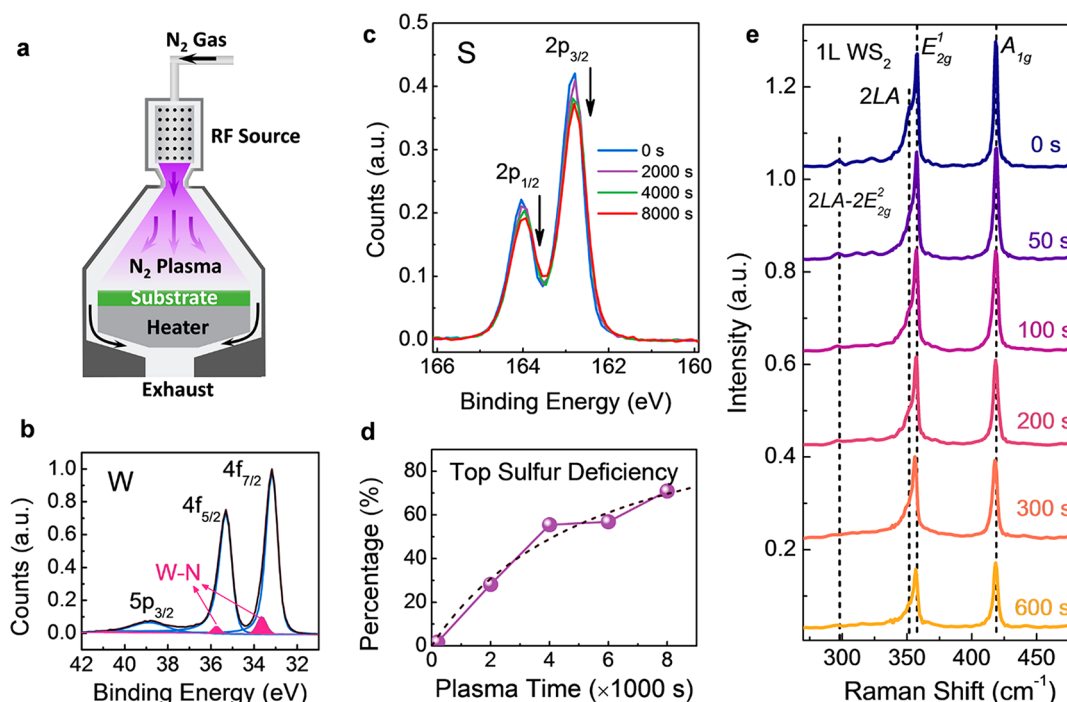
Figure 1. (a) Schematics of the remote plasma exposure system. (b) XPS signal of W core levels measured on the top surface of a large-area bulk WS_2 crystal after 8000 s remote N_2 plasma exposure. (c) XPS signals of S 2p core levels of bulk WS_2 surface with increasing plasma exposure time. The intensities of S 2p core levels are normalized by the corresponding W $4f_{7/2}$ peaks. (d) Extracted sulfur deficiency percentage of the top sulfur atom layer of bulk WS_2 as a function of plasma exposure time. (e) Raman spectra of exfoliated single-layer WS_2 with increasing remote N_2 plasma exposure.

In this work, we have conducted remote N_2 plasma exposure experiment on single-layer WS_2 and studied the defects generated, with an emphasis on their photoluminescence (PL) properties. A prominent low-energy PL peak is observed after short-time remote N_2 plasma exposure, the observation of which has a critical requirement on the plasma exposure dose. Through reference studies of remote Ar plasma exposure, in conjunction with the laser power dependence of PL, low-temperature PL, and first-principles calculations, this PL peak is attributed to defects related to the sulfur substitutions by nitrogen in single-layer WS_2. This N_2-plasma-induced low-energy PL peak can be used to monitor the covalent nitrogen doping concentration in single-layer WS_2. Our results also suggest that the substitutional nitrogen can potentially serve as an isolated artificial atom for creating single-photon emitters based on WS_2 with known defect type and emission wavelength.

RESULTS AND DISCUSSION

The system of plasma generation and exposure in our study is schematically shown in Figure 1a. Remote N_2 plasma is generated by an RF coil in a plasma-enhanced atomic layer deposition (PEALD) system (Kurt J. Lesker ALD 150LX Cluster Tool). The detailed plasma generation conditions can be found in the Methods section. After remote N_2 plasma treatment, sulfur substitution by nitrogen (N_S) is the most energetically favorable defect in TMDCs.[15−17] The stoichiometry changes of WS_2 after remote N_2 plasma exposure are investigated by X-ray photoelectron spectroscopy (XPS). Details on the XPS measurement setup can be found in the Methods section. The XPS measurement requires a relatively large sample area, but the mechanically exfoliated single-layer WS_2 is typically only a few micrometers in size. Considering

that the sulfur vacancies (V_S) and N_S defects on the surfaces of single-layer WS_2 and bulk WS_2 have similar formation energies (see Supporting Information (SI) Figure S1), the XPS measurements are conducted on a large cleaved surface of bulk WS_2 instead.

Figure 1b shows the XPS results of tungsten core levels after 8000 s N_2 plasma exposure. The collected XPS signals can originate from the bulk sample within a depth of 2−3 nm, but only the top surface bonds are modified by the mild remote N_2 plasma.[15] As a result, only a slight peak broadening of tungsten core levels is observed in Figure 1b, as caused by the formation of W−N bonds due to the sulfur substitutions by nitrogen at the top surface.[16] For the same reason, the XPS signals of sulfur core levels only show obvious drops after long-time plasma exposures, as shown in Figure 1c. XPS measurements are also attempted for large-area single-layer WS_2 grown by metalorganic chemical vapor deposition (MOCVD) method. A similar broadening of W 4f core levels is observed (see SI Figure S2). However, the sulfur to tungsten atomic ratio shows large random variations for MOCVD WS_2, which might be caused by the nonideal stoichiometry of WS_2 or some sulfur condensations after MOCVD growth. We note that the N 1s core level in XPS does not directly indicate the substitutional nitrogen concentrations in WS_2. Before remote N_2 plasma exposure, both the mechanically exfoliated and MOCVD-grown WS_2 samples are exposed to the ambient environment; thus organic contaminations are inevitable in our experiment, which are exposed to remote N_2 plasma as well, leading to a much higher XPS signal of N 1s core level than expected due to the nitridation of the organic contaminants (see SI Figure S3).[30]

The upper limit of substitutional nitrogen concentration in WS_2 can be estimated by the sulfur deficiencies, which are

contributed by both the nitrogen substitutions and the possible sulfur vacancies. The percentages of sulfur deficiencies can be derived from the drops of the XPS sulfur signals in Figure 1c. Assuming the sulfur deficiencies mostly occur at the top surface of bulk WS_2 and considering the S−W−S sandwich-like structure of each WS_2 layer, the sulfur deficiency percentages of bulk WS_2 surface are extracted in Figure 1d. The extraction details can be found in the SI. A fitted dashed curve in Figure 1d is plotted to guide the eye. According to the fitting, the sulfur deficiency percentage of the top atom layer gradually saturates and approaches around 100% after long-time plasma exposure, which is interpolated to be around 4.0% and 11.3% after 200 and 600 s remote N_2 plasma exposures, corresponding to 2.0% and 5.6% for the top WS_2 monolayer (S−W−S layers).

Because single-layer WS_2 and bulk WS_2 surfaces have very close defect formation energies (see SI Figure S1), it can be expected that similar defect densities will be created in single-layer WS_2 by remote N_2 plasma exposure. Single-layer WS_2 flakes are mechanically exfoliated on a SiO_2/Si substrate and exposed to remote N_2 plasma in the same plasma system as well. The exposed samples with various exposure doses are characterized by Raman spectroscopy excited by a 488 nm laser. The Raman spectra are normalized by the 520 cm^{-1} Si Raman peak and the phonon modes are assigned in Figure 1e.[31] Long N_2 plasma exposure time causes a clear drop of the Raman intensity and the smear-out of high-order Raman scattering peaks, as the crystalline single-layer WS_2 becomes defective. The possible defects are directly examined by atomic-resolution scanning transmission electron microscope (STEM). Clear nitrogen atom peak is observed in the energy-dispersive X-ray spectroscopy (EDS) measurement (see SI Figure S4), which could have extra contributions from the nitridized organic contaminations in addition to the nitrogen substitutions as well. No W vacancies or W antisite defects are created by the mild remote N_2 or Ar plasma. Other types of defects can be directly identified by STEM images, including single-sulfur vacancy, doule-sulfur vacancy, vacancy clusters, and mostly importantly, the nitrogen substitutions (see SI Figure S5).

PL can be a very sensitive tool to characterize the defects in TMDCs.[20−23,26] PL spectra of exfoliated single-layer WS_2 with increasing remote N_2 plasma exposure time are measured and plotted in logarithmic scale in Figure 2a. A 488 nm laser is used as the excitation. The measurements are conducted at room temperature and in the ambient environment. For the as-exfoliated single-layer WS_2, the PL spectrum is mainly contributed by neutral exciton (X^0), trion (X^T), and biexciton (XX) emissions at room temperature.[32,33] As shown in Figure 2a, remote N_2 plasma causes a decrease of PL intensity, typically due to the creation of defects.[20−22] Most interestingly, a short-time N_2 plasma exposure (<600 s) introduces a new PL peak at 1.59 eV (X^N), which reaches its strongest intensity with about 200 s exposure time. Nevertheless, its PL peak intensity is still only 10.4% of the corresponding exciton/trion/biexciton peak. Longer N_2 plasma exposure (≥600 s) on the contrary makes this peak weaker and finally unobservable. The same 1.59 eV PL peak after remote N_2 plasma exposure is observed for single-layer WS_2 grown on sapphire substrate by MOCVD method, as shown in Figure 2b. The sharp doublet at 1.786 and 1.789 eV is caused by the Cr^{3+} luminescence centers of the sapphire substrate for the MOCVD sample.[34] Different from the exfoliated samples (Figure 2a), the strong exciton/trion/
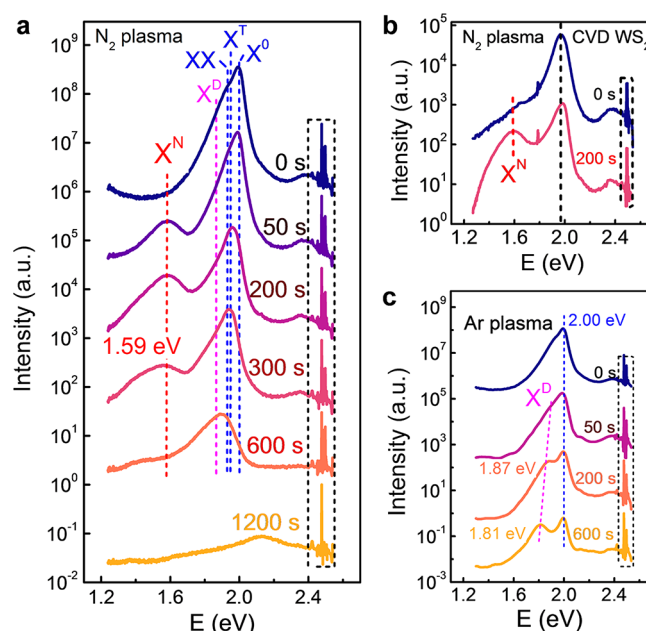

Figure 2. (a) PL spectra of exfoliated single-layer WS_2 after remote N_2 plasma exposure. A new PL peak X^N emerges at 1.59 eV after mild N_2 plasma treatment. (b) PL spectra of MOCVD-grown single-layer WS_2 before and after 200 s remote N_2 plasma exposure. The same 1.59 eV PL peak is observed. (c) PL spectra of exfoliated single-layer WS_2 after remote Ar plasma exposure. A different defect-related PL peak is observed instead. The PL intensities in (a−c) are all plotted in logarithmic scale to discern the relatively weak X^N peak and the PL spectra are shifted vertically for a clear view. The peaks in dashed squares of (a−c) are caused by Raman scattering.

biexciton peak of the MOCVD-grown single-layer WS_2 slightly blue shifts after remote N_2 plasma exposure, which might be related to the different initial doping conditions of MOCVD samples and needs further investigation.

Covalent nitrogen doping of WS_2 has been studied before, but no such 1.59 eV PL peak was reported.[17,24] One possible reason is that this PL peak is relatively weak compared to the strong exciton/trion/biexciton peak, which only becomes obvious when the spectrum is plotted in a logarithmic scale. Moreover, the observation of this PL peak has a critical requirement on the plasma dose. According to the XPS results, the 200 s N_2 plasma exposure with the strongest 1.59 eV PL peak corresponds to only 2.0% sulfur deficiency in single-layer WS_2, while 600 s N_2 plasma exposure (5.6% sulfur deficiency) has already quenched this PL peak. The relatively weak intensity of this new PL peak and its critical requirement on the low defect density may be the major reasons why other reports did not take notice of it.

Sulfur substitutions by nitrogen could be responsible for the emergent PL peak. As a further control experiment, remote Ar plasma is generated by the same PEALD system. PL spectra of single-layer WS_2 after the remote Ar plasma exposure are shown in Figure 2c. The corresponding Raman spectra are shown in SI Figure S6. As an inert gas, the mild remote Ar plasma exposure is believed to only sputter away atoms and tends to create sulfur vacancies.[22] Consistent with previous reports, the remote Ar plasma only introduces a PL peak (X^D) at around 1.81−1.87 eV,[22] distinct from the 1.59 eV PL peak caused by remote N_2 plasma. Considering other defects such as sulfur vacancies, antisites, interstitials, or their complex defect
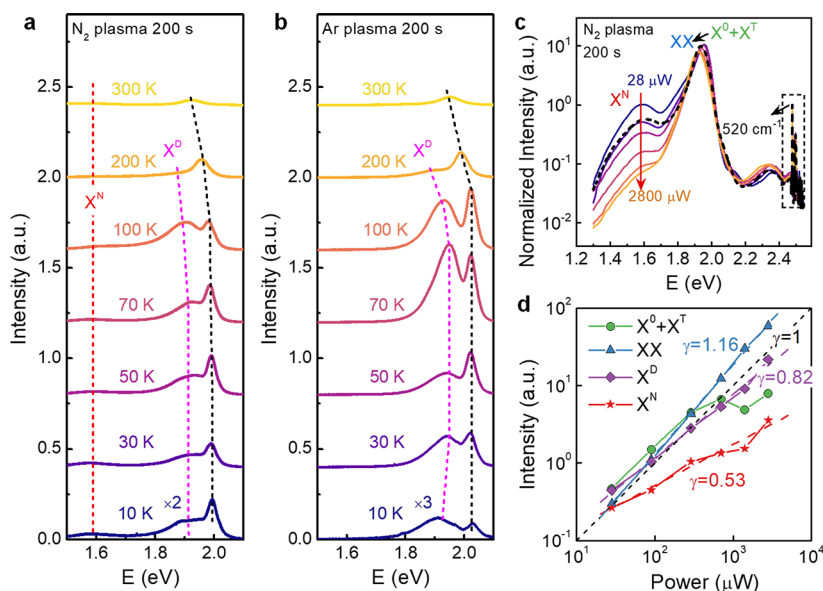
Figure 3. (a,b) PL spectra of exfoliated single-layer WS$_2$ measured at varied low temperatures after remote N$_2$ and Ar plasma exposures. The PL intensities are plotted in a linear scale for absolute intensity comparisons and shifted vertically for a clear view. Both N$_2$ and Ar plasma exposures lead to a defect-related PL peak X^D at low temperature. The N$_2$-plasma-induced PL peak X^N in (a) persists at low temperature. (c) PL spectra measured with increasing laser power for exfoliated single-layer WS$_2$ after 200 s remote N$_2$ plasma exposure, which are normalized by the 520 cm^{-1} Si Raman peaks. The black dashed line is a repeated measurement at 28 μW after large laser power excitations. (d) Extracted intensities of different PL components as a function of laser power.

clusters can be created by both N$_2$ and Ar plasma, this control experiment of Ar plasma suggests that the 1.59 eV PL peak induced by remote N$_2$ plasma exposure most likely originates from defects of sulfur substitutions by nitrogen, or at least from defect clusters involving nitrogen substitutions in single-layer WS$_2$. The energy of this PL peak is far away from the free exciton/trion/biexciton emissions, suggesting that the substitutional nitrogen defect of single-layer WS$_2$ can potentially serve as an isolated artificial atom to realize SPEs with high purity.[7]

Low-temperature PL measurement can reveal more and finer structures.[20,21,32] The PL spectra of single-layer WS$_2$ after remote N$_2$ and Ar plasma exposures are measured in Figure 3a,b respectively, which are plotted in linear scale for easy comparison of the absolute PL intensities. The ones plotted in logarithmic scale can be found in SI Figure S7. The N$_2$-plasma-induced PL peak (X^N) persists at low temperatures, and its wavelength shows relatively weak temperature dependence. Another PL peak (X^D), which becomes obvious at low temperatures, is similar for single-layer WS$_2$ after both remote N$_2$ and Ar plasma exposures, and shows obvious wavelength shift with measurement temperature. This X^D peak is most likely related to sulfur vacancies,[22] and its existence in N$_2$ exposed samples suggests that sulfur vacancies are probably not completely passivated by the substitutional nitrogen during remote N$_2$ plasma exposure (see SI Figure S5) or they are created by the mild dissociation of substitutional nitrogen atoms during the later laser excitations.

PL emissions of different origins can show distinct responses to laser power.[32,33] Figure 3c shows the PL spectra of exfoliated single-layer WS$_2$ after 200 s remote N$_2$ plasma exposure using different laser power excitations at room temperature. The PL spectra are all normalized by the 520 cm^{-1} Si Raman peak that changes almost linearly with laser power. The intensity of the 1.59 eV PL peak (X^N) clearly drops with the increasing laser power, indicating a decrease of emission efficiency at large laser power, which is typical for

defect-related PL due to the limited recombination defect centers.[32,33] After large power excitation (2800 μW), the PL spectrum is measured again with low power (28 μW), as shown by the black dashed line in Figure 3c. The 1.59 eV PL peak only becomes slightly weaker after laser heating, which might be related to the mild dissociations of substitutional nitrogen and indicates the relatively good stability of the responsible defects. Consistent with previous reports,[32,33] the large laser power excitation causes a gradual shift of trion/exciton emission toward biexciton emission (Figure 3c). As a result, the biexciton peak exhibits a superlinear relationship ($\gamma > 1$) between PL intensities I and laser power P ($I \propto P^\gamma$), as extracted by Gaussian fittings and plotted in Figure 3d. The fitting details can be found in the Methods sections. A sublinear relationship ($\gamma < 1$) between PL intensities and laser power is also observed for both the 1.59 eV PL peak X^N and the defect-related peak X^D, as expected for the defect-limited emissions.[32,33]

First-principles calculations have been used to better understand the electronic band structures and the optical responses of 2D semiconductors with defects.[13,27−29,35−37] As discussed above, the new PL peak X^N emerging after remote N$_2$ plasma exposure is most likely contributed by the substitutional nitrogen defect (N_S). To further verify this, density functional theory (DFT) and many-body perturbation theories are used to investigate the electronic and optical properties of single-layer WS$_2$, as implemented by Quantum ESPRESSO and BerkeleyGW packages.[38,39] Quantum ESPRESSO returns the self-consistent wave functions and eigenvalues by solving the Kohn−Sham (KS) equation. As widely known, it tends to underestimate the bandgap.[36,37] To overcome this issue, many-body effects can be included by a subsequent GW calculation, and then quasiparticle energies can be obtained.[27,35−37] A fully self-consistent GW calculation can be quite time-consuming and computational-resource demanding. Moreover, it also tends to significantly over-
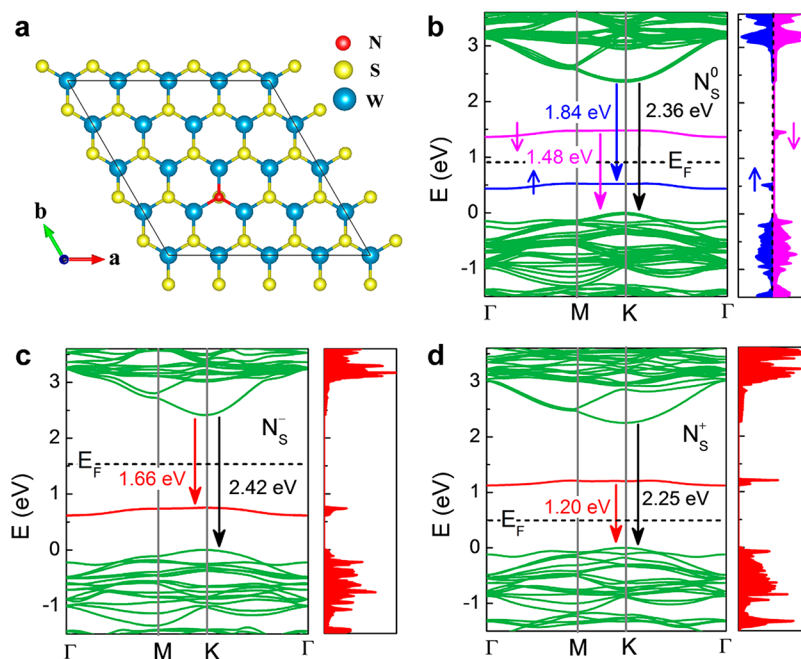
Figure 4. (a) Atomic structure of the 4 × 4 supercell used in the GW-BSE calculations, with one top sulfur atom of of single-layer WS$_2$ substituted by nitrogen. (b−d) Single-shot GW (G_0W_0) quasiparticle band diagrams and the corresponding densities of states of the N-substituted WS$_2$ at neutral (N_S^0), negative (N_S^-), and positive (N_S^+) charge states. The up and down arrows in (b) are for spin-up and spin-down electrons, respectively. The Fermi level positions are indicated by the black dashed lines.
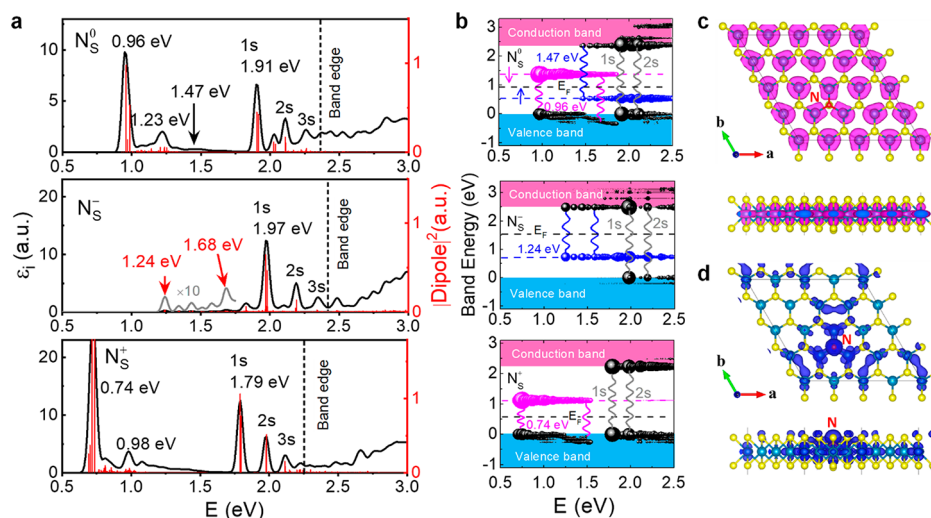

Figure 5. (a) Imaginary permittivities and the exciton oscillator strengths of the nitrogen-substituted single-layer WS$_2$ at different charge states, solved by Bethe-Salpeter equation (BSE) based on G_0W_0 results. (b) Band contributions to the corresponding excitons in (a). The major electron−hole pairs are indicated by the vertical wavy lines. The contributions of the occupied defect band are in blue and the contributions of the unoccupied defect band are in magenta. To highlight the contributions of the concerned excitons with substantially strong optical absorptions, the size of each dot is proportional to both its exciton contribution and the square root of the corresponding exciton dipole. Top and side views of (c) the integrated electron wave function and (d) the integrated hole wave function for the 1.24 eV exciton of N_S^- defect in (a).

estimate the bandgaps of semiconductors.[36] Various perturbative approximations for GW calculations can be used instead. Single-shot GW (G_0W_0) calculation can give reasonable bandgaps and thus is adopted here,[36] as implemented in the BerkeleyGW package. The calculation details can be found in the Methods section.

Figure 4a shows the 4 × 4 supercell of single-layer WS$_2$ used in the calculations, with one top sulfur atom substituted by nitrogen. The quasiparticle band diagrams of single-layer WS$_2$ with the substitutional nitrogen defect at different charge states

are calculated in Figure 4b−d. Atomic structures are relaxed for all charged defects while the supercell size is maintained as that of pristine WS$_2$, which is reasonable for our samples on a solid substrate. As shown in Figure 4b, the calculated GW bandgap ignoring the defect levels for WS$_2$ with neutral defect (N_S^0) is about 2.36 eV, very close to the experimentally measured 2.41 eV.[1] N_S^0 defect has an unpaired electron due to the neutral nitrogen atom and thus is spin-polarized.[37,40] For charged defects, the addition or removal of one electron significantly changes the quasiparticle defect levels, as shown in

Figure 4c-d. The bandgap also varies for the different charged defects, especially for N_S^+ defect, due to the limited 4×4 supercell used here as constrained by the computational-resource demanding GW and BSE calculations. Some possible transitions between the occupied and unoccupied bands at the K point for these defects are indicated by the vertical arrows with labeled energies. The transition between the unoccupied spin-down defect level to the valence band maximum shows the energy of 1.48 eV for N_S^0 defect, while the transition between the conduction band minimum to the occupied defect level for N_S^- defect shows energy of 1.66 eV. Both are close to the experimentally observed 1.59 eV low-energy PL peak after remote N_2 plasma exposure.

The quasiparticle transition energy has not considered the Coulomb or exchange interactions between the electron and hole pairs, i.e. the exciton binding energy. As a result, it may be not accurate to account for the experimental results. Especially for 2D semiconductors, because of the reduced dielectric screening, the exciton binding energy should not be ignored.[1,3,27,36] The exciton binding energy can be included in the GW quasiparticle energies by a subsequent Bethe-Salpeter equation (BSE) calculation,[27,36] which will return all the possible excitons formed between the considered occupied and unoccupied bands. Using the G_0W_0 results in Figure 4b−d as the starting point, the BSE imaginary permittivities and exciton oscillator strengths of the substitutional nitrogen defect at different charge states are calculated in Figure 5a. The envelopes of the labeled exciton series are identified according to their electron−hole-pair amplitudes in reciprocal space. The corresponding results for pristine single-layer WS_2 are shown in SI Figure S8 as references. The calculated 1s free exciton energy of the neutral defect is close to the 2.00 eV of A exciton in the experiment, while those of charged defects show variations, due to the charge effect and the limited 4×4 supercell size used here.[35,36,41] Very similar shift trends are observed in the rough GW-BSE calculations based on Vienna *ab initio* simulation package (VASP), without using the advanced convergence techniques such as the dual-grid interpolations,[42] k-point subsampling,[43] and Coulomb inter-action truncations that are included in BerkeleyGW package (see SI Figure S9).[38,44]

The imaginary permittivity is closely related to the photon absorptions and possible emissions.[26,35] Some low-energy exciton peaks with relatively strong absorptions are marked in Figure 5a. To identify the band contributions to a specific exciton, the wave function $\Phi^n(r_e, r_h)$ of the nth exciton can be written into contributions of different electron and hole pairs formed between the unoccupied and occupied bands,[45,46]

$$\Phi^n(r_e, r_h) = \sum_c \sum_v \sum_k A_{cvk}^n \phi_{ck}(r_e)\phi_{vk}^*(r_h) \tag{1}$$

in which r_e and r_h are the electron and hole coordinates respectively, $\phi_{ck}(r_e)$, and $\phi_{vk}(r_h)$ are the wave functions of the unoccupied band c and occupied band v at k-point k, and A_{cvk}^n is the corresponding weight of this electron and hole pair. The summations are for the considered unoccupied and occupied bands in the first Brillouin zone. To evaluate the contributions of a specific band to the nth exciton, the contributions of all wave functions $\phi_{ck}(r_e)$ in conduction band c can be calculated by $\sum_{vk}|A_{cvk}^n|^2$. Similarly, the contributions of all wave functions $\phi_{vk}(r_h)$ in valence band v can be calculated by $\sum_{ck}|A_{cvk}^n|^2$.

The band contributions of the exciton peaks in Figure 5a are calculated and plotted in Figure 5b. It can be seen that the low-

energy excitons are mainly formed by the unoccupied defect level and the valence band, or by the occupied defect level and the conduction band. For N_S^0 and N_S^+ defects, a very strong absorption (0.96 and 0.74 eV respectively) can be observed due to the excitons formed by the unoccupied defect level and the valence band. These excitons are in the infrared region and the related possible emissions are not in our measurement range. Interestingly, two kinds of defect excitons, involving the unoccupied and occupied defect levels respectively, can coexist in the N_S^0 defect, as can be seen in the upper panel of Figure 5b, even though the dipoles of excitons formed by the occupied defect level and conduction band are much weaker. The detailed electron−hole pair amplitudes for these excitons of N_S^0 defect in reciprocal space can be found in SI Figure S10.

In the experiment, the as-prepared WS_2 tends to be naturally *n*-type doped.[17,47] After the sulfur substitution by nitrogen, at least a portion of the substitutional nitrogen defects should be negatively charged, due to the electron transfer from the conduction band to the deep nitrogen defect levels. At low substitutional nitrogen concentration, we can expect that the major nitrogen defects should be N_S^-. As shown in the middle panels of Figure 5a,b for N_S^- defect, the lowest-energy exciton formed between the conduction band and the occupied defect level has the energy of 1.24 eV, meaning a binding energy of 0.42 eV, compared to the free transition energy of 1.66 eV in Figure 4c. The integrated electron and hole wave functions for the 1.24 eV exciton of N_S^- defect are plotted in Figure 5c,d. As expected, the integrated hole wave function is localized near the substitutional nitrogen atom, since it is mainly contributed by the occupied localized defect level. Besides the lowest-energy exciton, some higher-energy exciton series can be found, with energies closer to the experimental 1.59 eV of low-energy PL peak. Considering the natural doping conditions and the calculated exciton series of the N_S^- defect near 1.59 eV, the negatively charged substitutional nitrogen is the probable defect responsible for the low-energy PL peak of single-layer WS_2 after nitrogen plasma exposure in our experiment. Assuming the many excitons formed between the conduction band and the occupied defect level are similar to the free exciton series (1s, 2s, 3s etc.), the lowest-energy 1.24 eV exciton should also be easier to be observed during PL emission. The discrepancies between experiment and theory could be partly due to the limitations of DFT calculations, since the strongly localized defect states are involved here and it is well-known that the density functional often fails to deal with strongly localized system and shows concave or convex approximation errors.[40,48] Besides, WS_2 has a strong spin−orbit coupling, which is not considered here due to its formidable computational resource requirements.

CONCLUSIONS

In summary, we have discovered and studied the remote N_2 plasma induced PL peak in single-layer WS_2, which is observed for both the mechanically exfoliated and MOCVD-grown WS_2. This new PL peak has a critical requirement on the plasma exposure dose, which is strongest at 2.0% sulfur deficiency and vanishes at 5.6%. This PL has a defect origin, as supported by the sublinear relationship between the laser power and PL intensity. Even though low-temperature PL reveals that sulfur vacancies are probably also present in single-layer WS_2 after remote N_2 plasma exposure, no such PL peak is observed for remote Ar plasma exposure, suggesting that defects related to nitrogen substitutions are probably responsible for this peak.

First-principles calculations including the many-body effect, electron–hole exchange, and Coulomb interactions are conducted, revealing that the substitutional nitrogen defect, especially the negatively charged substitutional nitrogen defect (N_S^-) could create exciton transitions between the conduction band and the occupied defect level, and are potential origins of this new PL peak. Other possible defect clusters involving nitrogen substitutions, such as N_S with adjacent V_S defect, are currently not ruled out yet and deserve further in-depth investigations. Our experimental results are a significant step toward the defect photoluminescence study of 2D semiconductors, which can be used to monitor the substitution nitrogen defect densities in single-layer WS_2. Moreover, the defect-related bound excitons caused by the substitutional nitrogen in single-layer WS_2 can find potential applications in single-photon emitters with a known defect type and controlled emission wavelength. Further investigations about the optical valley selectivity, spin read-out, and manipulation capabilities of the substitutional nitrogen defect, and the explorations of other similar defects such as phosphorus substitutions are worth conducting in the future.

METHODS

Sample Preparations. Single-layer WS_2 flakes (HQ graphene) were mechanically exfoliated on Si substrate capped with 300 nm SiO_2. The single-layer WS_2 flakes were identified by the color contrast and also the exceptional strong PL intensity compared with multilayer WS_2.[49] For MOCVD growth of single-layer WS_2, a cold-wall, horizontal, low-pressure MOCVD reactor was employed, with $W(CO)_6$ and H_2S as the tungsten and sulfur precursors.[47] After preparations, WS_2 samples were treated by remote N_2 plasma or Ar plasma, which was generated in a PEALD system (Kurt J. Lesker ALD 150LX Cluster Tool). Remote N_2 plasma was generated by the RF coil using 25 sccm N_2 as the source. The pressure was 96 mTorr and the RF power was fixed at 25 W. For Ar plasma generation, the Ar flow rate was 75 sccm, the pressure was 430 mTorr, and the RF power was 50 W. The substrate temperature was fixed at 110 °C.

Characterization. XPS experiments were performed using a Physical Electronics VersaProbe II instrument equipped with a monochromatic Al kα X-ray source ($h\nu$ = 1486.7 eV) and a concentric hemispherical analyzer. Charge neutralization was performed using both low-energy electrons (<5 eV) and argon ions. The binding energy axis was calibrated using sputter cleaned Cu (Cu $2p_{3/2}$ = 932.62 eV, Cu $3p_{3/2}$ = 75.1 eV) and Au foils (Au $4f_{7/2}$ = 83.96 eV). Measurements were made at a takeoff angle of 45°. The room-temperature Raman spectra and PL were measured by Horiba LabRam HR Evolution confocal microscope in the backscattering geometry equipped with 600 gr/nm and 1800 gr/nm, respectively. A 488 nm laser was used as excitation, with a 100× objective. The laser spot has a diameter of about 1 μm. During the Gaussian fitting of the laser-power-dependent room-temperature PL, a fitting of the PL at the lowest laser power is conducted first with all the fitting parameters free. Because the defect-related PL is still relatively strong at low laser power, the fitting is more trustworthy and the fitted peak positions are consistent with previous reports. For PL with increasing laser power, to avoid the drastic shift of the defect-related PL peak positions due to its weak or even barely visible intensities, the peak positions of all the PL components are then kept fixed. Low-temperature PL spectra were measured by cooling the sample in a home-built liquid helium cryostat to 10 K. A 400 nm continuous-wave (CW) laser was used to excite WS_2. PL was recorded using Princeton Instruments' SpectraPro HRS-750 together with a CCD cooled by liquid nitrogen.

First-Principles Calculations. *Ab initio* GW and Bethe–Salpeter equation (GW-BSE) calculations are conducted to determine the quasiparticle band structures and the optical absorption spectra. Quantum ESPRESSO and BerkeleyGW packages are used.[38,39] Quantum ESPRESSO is used to generate the mean-field charge densities, wave functions, and eigenvalues, which are used by BerkeleyGW subsequently to calculate the GW self-energy and BSE absorptions. PBE-optimized norm-conserving Vanderbilt pseudopotentials are used,[50] with a kinetic energy cutoff of 40 Ry. W 4f, 5s, 5p semicores, and 5d, 6s valence electrons are included in the pseudopotentials. The inclusion of semicore states is intended to accurately calculate the exchange contribution to the GW self-energy.[51] However, the semicore electrons are not included in the charge density in the Hybertsen-Louie generalized plasmon pole (HL-GPP) model,[52] since they are lying deep below the Fermi level and not contributing to the screening.[51] A 4 × 4 supercell of single-layer WS_2 with one top sulfur atom substituted by nitrogen was adopted here to simulate the remote N_2 plasma-treated WS_2. To calculate the GW quasiparticle energy, a dielectric matrix cutoff of 15 Ry, a 4 × 4 × 1 k-mesh with 10 q-point nonuniform neck subsampling (NNS) along (110) direction and 1600 bands are used during the summation. Similar parameters are used in another publication to guarantee the convergence.[27] The quasiparticle band diagram is obtained by interpolating along high symmetry lines using the maximally localized Wannier functions (MLWFs) through Wannier90 code.[53] During the BSE calculation, the quasiparticle energies, direct and exchange kernels of a 6 × 6 × 1 coarse k-mesh are interpolated onto a fine 18 × 18 × 1 k-mesh, together with cluster sampling interpolation (CSI) using a subfactor of 3 along (110) direction. The BSE equation is then solved by direct diagonalization within the Tamm–Dancoff approximation. About 16 valence and 16 conduction bands on the fine k-mesh grid are included, interpolated from about 36 valence and 36 conduction bands on the coarse k-mesh. The exact band numbers are slightly dependent on the band degeneracy conditions for different charged defects. The nonlocal part of the pseudopotential to the dipole transition matrix elements is considered. 2D slab truncation of Coulomb interaction is used.[44]

ASSOCIATED CONTENT

ⓢ Supporting Information

The Supporting Information is available free of charge at https://pubs.acs.org/doi/10.1021/acsnano.1c09809.

Defect formation energies of 1L and 3L WS_2; XPS of single-layer WS_2 grown by MOCVD on the sapphire substrate; XPS N 1s core levels of bulk WS_2 treated by N_2 plasma; extraction of sulfur deficiencies on the top surface of bulk WS_2 based on XPS results of sulfur core levels; STEM measurements and defect identifications of N_2 plasma treated single-layer WS_2; Raman spectra of single-layer WS_2 after remote Ar plasma treatment; low temperature PL spectra plotted in logarithmic scale; GW-BSE results for pristine 1 × 1 WS_2; rough estimations of GW-BSE done by Vienna *ab initio* simulation package (VASP); electron–hole pair amplitudes in reciprocal space for excitons of N_S^0 defect (PDF)

AUTHOR INFORMATION

Corresponding Authors

Qingkai Qian — *Key Laboratory of Optoelectronic Technology and System (Ministry of Education), College of Optoelectronic Engineering, Chongqing University, Chongqing 400044, China; Department of Electrical Engineering, The Pennsylvania State University, University Park, Pennsylvania 16802, United States;* ⓞ orcid.org/0000-0001-7513-0676; Email: qqian@cqu.edu.cn

Shengxi Huang — *Department of Electrical Engineering, The Pennsylvania State University, University Park, Pennsylvania 16802, United States;* ⓞ orcid.org/0000-0002-3618-9074; Email: sjh5899@psu.edu

Authors

Wenjing Wu — *Department of Electrical Engineering, The Pennsylvania State University, University Park, Pennsylvania 16802, United States*

Lintao Peng — *Center for Nanoscale Materials, Argonne National Laboratory, Argonne, Illinois 60439, United States*

Yuanxi Wang — *Department of Physics, The Pennsylvania State University, University Park, Pennsylvania 16802, United States;* ⊙ orcid.org/0000-0002-0659-1134

Anne Marie Z. Tan — *Department of Materials Science and Engineering, University of Florida, Gainesville, Florida 32611, United States; School of Mechanical and Aerospace Engineering, Nanyang Technological University, Singapore 639798, Singapore; Present Address: Institute of High Performance Computing, A*STAR, Singapore 138632, Singapore*

Liangbo Liang — *Center for Nanophase Materials Sciences, Oak Ridge National Laboratory, Oak Ridge, Tennessee 37831, United States;* ⊙ orcid.org/0000-0003-1199-0049

Saban M. Hus — *Center for Nanophase Materials Sciences, Oak Ridge National Laboratory, Oak Ridge, Tennessee 37831, United States*

Ke Wang — *Materials Research Institute, The Pennsylvania State University, University Park, Pennsylvania 16802, United States*

Tanushree H. Choudhury — *2D Crystal Consortium, Materials Research Institute, The Pennsylvania State University, University Park, Pennsylvania 16802, United States;* ⊙ orcid.org/0000-0002-0662-2594

Joan M. Redwing — *2D Crystal Consortium, Materials Research Institute and Department of Materials Science and Engineering, The Pennsylvania State University, University Park, Pennsylvania 16802, United States;* ⊙ orcid.org/0000-0002-7906-452X

Alexander A. Puretzky — *Center for Nanophase Materials Sciences, Oak Ridge National Laboratory, Oak Ridge, Tennessee 37831, United States;* ⊙ orcid.org/0000-0002-9996-4429

David B. Geohegan — *Center for Nanophase Materials Sciences, Oak Ridge National Laboratory, Oak Ridge, Tennessee 37831, United States*

Richard G. Hennig — *Department of Materials Science and Engineering, University of Florida, Gainesville, Florida 32611, United States;* ⊙ orcid.org/0000-0003-4933-7686

Xuedan Ma — *Center for Nanoscale Materials, Argonne National Laboratory, Argonne, Illinois 60439, United States*

Complete contact information is available at:
https://pubs.acs.org/10.1021/acsnano.1c09809

Author Contributions

The manuscript was written through the contributions of all authors. All authors have approved the final version of the manuscript. Q.Q. carried out the mechanical exfoliations and conducted the XPS, room-temperature Raman scattering and room-temperature PL measurements. W.W. prepared the STEM samples and K.W. conducted the STEM characterizations. T.H.C. prepared the MOCVD WS$_2$ samples. Q.Q., L.P., and A.A.P. measured the low-temperature PL. Q.Q. carried out the data analysis and theoretical calculations. Q.Q., Y.W., A.M.Z.T, L.L., S.M.H., J.M.R., A.A.P., D.B.G., R.G.H, X.M., and S.H. discussed the results. The work was conceived and supervised by J.M.R., A.A.P., D.B.G., R.G.H., X.M., and S.H..

Notes

The authors declare no competing financial interest.

REFERENCES

(1) Chernikov, A.; Berkelbach, T. C.; Hill, H. M.; Rigosi, A.; Li, Y.; Aslan, O. B.; Reichman, D. R.; Hybertsen, M. S.; Heinz, T. F. Exciton Binding Energy and Nonhydrogenic Rydberg Series in Monolayer WS$_2$. *Phys. Rev. Lett.* **2014**, *113*, 76802.

(2) Bernardi, M.; Palummo, M.; Grossman, J. C. Extraordinary Sunlight Absorption and One Nanometer Thick Photovoltaics Using Two-Dimensional Monolayer Materials. *Nano Lett.* **2013**, *13*, 3664−3670.

(3) He, K.; Kumar, N.; Zhao, L.; Wang, Z.; Mak, K. F.; Zhao, H.; Shan, J. Tightly Bound Excitons in Monolayer WSe$_2$. *Phys. Rev. Lett.* **2014**, *113*, 26803.

(4) Liu, X.; Hersam, M. C. 2D Materials for Quantum Information Science. *Nat. Rev. Mater.* **2019**, *4*, 669−684.

(5) Tsai, M.; Su, S.; Chang, J.; Tsai, D.; Chen, C.; Wu, C.; Li, L.; Chen, L.; He, J. Monolayer MoS$_2$ Heterojunction Solar Cells. *ACS Nano* **2014**, *8*, 8317−8322.

(6) Baugher, B. W. H.; Churchill, H. O. H.; Yang, Y.; Jarillo-Herrero, P. Optoelectronic Devices Based on Electrically Tunable *p-n* Diodes in a Monolayer Dichalcogenide. *Nat. Nanotechnol.* **2014**, *9*, 262−267.

(7) Toth, M.; Aharonovich, I. Single Photon Sources in Atomically Thin Materials. *Annu. Rev. Phys. Chem.* **2019**, *70*, 123−142.

(8) Schaibley, J. R.; Yu, H.; Clark, G.; Rivera, P.; Ross, J. S.; Seyler, K. L.; Yao, W.; Xu, X. Valleytronics in 2D Materials. *Nat. Rev. Mater.* **2016**, *1*, 16055.

(9) Mak, K. F.; He, K.; Shan, J.; Heinz, T. F. Control of Valley Polarization in Monolayer MoS$_2$ by Optical Helicity. *Nat. Nanotechnol.* **2012**, *7*, 494−498.

(10) Zeng, H.; Dai, J.; Yao, W.; Xiao, D.; Cui, X. Valley Polarization in MoS$_2$ Monolayers by Optical Pumping. *Nat. Nanotechnol.* **2012**, *7*, 490−493.

(11) Branny, A.; Kumar, S.; Proux, R.; Gerardot, B. D. Deterministic Strain-Induced Arrays of Quantum Emitters in a Two-Dimensional Semiconductor. *Nat. Commun.* **2017**, *8*, 15053.

(12) Tonndorf, P.; Del Pozo-Zamudio, O.; Gruhler, N.; Kern, J.; Schmidt, R.; Dmitriev, A. I.; Bakhtinov, A. P.; Tartakovskii, A. I.; Pernice, W.; Michaelis De Vasconcellos, S.; Bratschitsch, R. On-Chip Waveguide Coupling of a Layered Semiconductor Single-Photon Source. *Nano Lett.* **2017**, *17*, 5446−5451.

(13) Tran, T. T.; Bray, K.; Ford, M. J.; Toth, M.; Aharonovich, I. Quantum Emission from Hexagonal Boron Nitride Monolayers. *Nat. Nanotechnol.* **2016**, *11*, 37−41.

(14) He, Y.; Clark, G.; Schaibley, J. R.; He, Y.; Chen, M.; Wei, Y.; Ding, X.; Zhang, Q.; Yao, W.; Xu, X.; Lu, C.; Pan, J. Single Quantum Emitters in Monolayer Semiconductors. *Nat. Nanotechnol.* **2015**, *10*, 497−502.

(15) Azcatl, A.; Qin, X.; Prakash, A.; Zhang, C.; Cheng, L.; Wang, Q.; Lu, N.; Kim, M. J.; Kim, J.; Cho, K.; Addou, R.; Hinkle, C. L.; Appenzeller, J.; Wallace, R. M. Covalent Nitrogen Doping and Compressive Strain in MoS$_2$ by Remote N$_2$ Plasma Exposure. *Nano Lett.* **2016**, *16*, 5437−5443.

(16) Khosravi, A.; Addou, R.; Smyth, C. M.; Yue, R.; Cormier, C. R.; Kim, J.; Hinkle, C. L.; Wallace, R. M. Covalent Nitrogen Doping in Molecular Beam Epitaxy-Grown and Bulk WSe$_2$. *APL Mater.* **2018**, *6*, 26603.

(17) Tang, B.; Yu, Z. G.; Huang, L.; Chai, J.; Wong, S. L.; Deng, J.; Yang, W.; Gong, H.; Wang, S.; Ang, K.; Zhang, Y.; Chi, D. Direct *n*- to *p*-Type Channel Conversion in Monolayer/Few-Layer WS$_2$ Field-Effect Transistors by Atomic Nitrogen Treatment. *ACS Nano* **2018**, *12*, 2506−2513.

(18) Nipane, A.; Karmakar, D.; Kaushik, N.; Karande, S.; Lodha, S. Few-Layer MoS$_2$ *p*-Type Devices Enabled by Selective Doping Using Low Energy Phosphorus Implantation. *ACS Nano* **2016**, *10*, 2128−2137.

(19) Kozhakhmetov, A.; Schuler, B.; Tan, A. M. Z.; Cochrane, K. A.; Nasr, J. R.; El Sherif, H.; Bansal, A.; Vera, A.; Bojan, V.; Redwing, J. M.; Bassim, N.; Das, S.; Hennig, R. G.; Weber Bargioni, A.; Robinson, J. A. Scalable Substitutional Re-Doping and its Impact on the Optical and Electronic Properties of Tungsten Diselenide. *Adv. Mater.* **2020**, *32*, 2005159.

(20) Wu, Z.; Zhao, W.; Jiang, J.; Zheng, T.; You, Y.; Lu, J.; Ni, Z. Defect Activated Photoluminescence in WSe$_2$ Monolayer. *J. Phys. Chem. C* **2017**, *121*, 12294−12299.

(21) Qian, Q.; Peng, L.; Perea-Lopez, N.; Fujisawa, K.; Zhang, K.; Zhang, X.; Choudhury, T. H.; Redwing, J. M.; Terrones, M.; Ma, X.; Huang, S. Defect Creation in WSe$_2$ with a Microsecond Photoluminescence Lifetime by Focused Ion Beam Irradiation. *Nanoscale* **2020**, *12*, 2047−2056.

(22) Chow, P. K.; Jacobs-Gedrim, R. B.; Gao, J.; Lu, T.; Yu, B.; Terrones, H.; Koratkar, N. Defect-Induced Photoluminescence in Monolayer Semiconducting Transition Metal Dichalcogenides. *ACS Nano* **2015**, *9*, 1520−1527.

(23) Wu, Z.; Luo, Z.; Shen, Y.; Zhao, W.; Wang, W.; Nan, H.; Guo, X.; Sun, L.; Wang, X.; You, Y.; Ni, Z. Defects as a Factor Limiting Carrier Mobility in WSe$_2$: A Spectroscopic Investigation. *Nano Res.* **2016**, *9*, 3622−3631.

(24) Cao, Q.; Dai, Y.; Xu, J.; Chen, L.; Zhu, H.; Sun, Q.; Zhang, D. W. Realizing Stable *p*-Type Transporting in Two-Dimensional WS$_2$ Films. *ACS Appl. Mater. Interfaces* **2017**, *9*, 18215−18221.

(25) Refaely-Abramson, S.; Qiu, D. Y.; Louie, S. G.; Neaton, J. B. Defect-Induced Modification of Low-Lying Excitons and Valley Selectivity in Monolayer Transition Metal Dichalcogenides. *Phys. Rev. Lett.* **2018**, *121*, 167402.

(26) Moody, G.; Tran, K.; Lu, X.; Autry, T.; Fraser, J. M.; Mirin, R. P.; Yang, L.; Li, X.; Silverman, K. L. Microsecond Valley Lifetime of Defect-Bound Excitons in Monolayer WSe$_2$. *Phys. Rev. Lett.* **2018**, *121*, 57403.

(27) Zheng, Y. J.; Chen, Y.; Huang, Y. L.; Gogoi, P. K.; Li, M.; Li, L.; Trevisanutto, P. E.; Wang, Q.; Pennycook, S. J.; Wee, A. T. S.; Quek, S. Y. Point Defects and Localized Excitons in 2D WSe$_2$. *ACS Nano* **2019**, *13*, 6050−6059.

(28) Weston, L.; Wickramaratne, D.; Mackoit, M.; Alkauskas, A.; Van de Walle, C. G. Native Point Defects and Impurities in Hexagonal Boron Nitride. *Phys. Rev. B* **2018**, *97*, 214104.

(29) Gupta, S.; Yang, J.; Yakobson, B. I. Two-Level Quantum Systems in Two-Dimensional Materials for Single Photon Emission. *Nano Lett.* **2019**, *19*, 408−414.

(30) Lobato, I.; Van Dyck, D. MULTEM: A New Multislice Program to Perform Accurate and Fast Electron Diffraction and Imaging Simulations Using Graphics Processing Units with CUDA. *Ultramicroscopy* **2015**, *156*, 9−17.

(31) Berkdemir, A.; Gutiérrez, H. R.; Botello-Méndez, A. R.; Perea-López, N.; Elías, A. L.; Chia, C.; Wang, B.; Crespi, V. H.; López-Urías, F.; Charlier, J.; Terrones, H.; Terrones, M. Identification of Individual and Few Layers of WS$_2$ Using Raman Spectroscopy. *Sci. Rep.* **2013**, *3*, 1755.

(32) Shang, J.; Shen, X.; Cong, C.; Peimyoo, N.; Cao, B.; Eginligil, M.; Yu, T. Observation of Excitonic Fine Structure in a 2D Transition-Metal Dichalcogenide Semiconductor. *ACS Nano* **2015**, *9*, 647−655.

(33) Paradisanos, I.; Germanis, S.; Pelekanos, N. T.; Fotakis, C.; Kymakis, E.; Kioseoglou, G.; Stratakis, E. Room Temperature Observation of Biexcitons in Exfoliated WS$_2$ Monolayers. *Appl. Phys. Lett.* **2017**, *110*, 193102.

(34) Dumcenco, D.; Ovchinnikov, D.; Lopez Sanchez, O.; Gillet, P.; Alexander, D. T. L.; Lazar, S.; Radenovic, A.; Kis, A. Large-Area MoS$_2$ Grown Using H$_2$S as the Sulphur Source. *2D Mater.* **2015**, *2*, 44005.

(35) Chen, W.; Pasquarello, A. Correspondence of Defect Energy Levels in Hybrid Density Functional Theory and Many-Body Perturbation Theory. *Phys. Rev. B* **2013**, *88*, 115104.

(36) Chen, W.; Pasquarello, A. First-Principles Determination of Defect Energy Levels through Hybrid Density Functionals and GW. *J. Phys.: Condens. Matter* **2015**, *27*, 133202.

(37) Hwang, J.; Zhang, C.; Kim, Y.; Wallace, R. M.; Cho, K. Giant Renormalization of Dopant Impurity Levels in 2D Semiconductor MoS$_2$. *Sci. Rep.* **2020**, *10*, 4938.

(38) Deslippe, J.; Samsonidze, G.; Strubbe, D. A.; Jain, M.; Cohen, M. L.; Louie, S. G. BerkeleyGW: A Massively Parallel Computer Package for the Calculation of the Quasiparticle and Optical Properties of Materials and Nanostructures. *Comput. Phys. Commun.* **2012**, *183*, 1269−1289.

(39) Giannozzi, P.; Baroni, S.; Bonini, N.; Calandra, M.; Car, R.; Cavazzoni, C.; Ceresoli, D.; Chiarotti, G. L.; Cococcioni, M.; Dabo, I.; Dal Corso, A.; de Gironcoli, S.; Fabris, S.; Fratesi, G.; Gebauer, R.; Gerstmann, U.; Gougoussis, C.; Kokalj, A.; Lazzeri, M.; Martin-Samos, L.; et al. QUANTUM ESPRESSO: A Modular and Open-Source Software Project for Quantum Simulations of Materials. *J. Phys.: Condens. Matter* **2009**, *21*, 395502.

(40) Bruneval, F. GW Approximation of the Many-Body Problem and Changes in the Particle Number. *Phys. Rev. Lett.* **2009**, *103*, 176403.

(41) Komsa, H.; Rantala, T. T.; Pasquarello, A. Finite-Size Supercell Correction Schemes for Charged Defect Calculations. *Phys. Rev. B* **2012**, *86*, 45112.

(42) Rohlfing, M.; Louie, S. G. Electron-Hole Excitations and Optical Spectra From First Principles. *Phys. Rev. B* **2000**, *62*, 4927.

(43) Da Jornada, F. H.; Qiu, D. Y.; Louie, S. G. Nonuniform Sampling Schemes of the Brillouin Zone for Many-Electron Perturbation-Theory Calculations in Reduced Dimensionality. *Phys. Rev. B* **2017**, *95*, 35109.

(44) Ismail-Beigi, S. Truncation of Periodic Image Interactions for Confined Systems. *Phys. Rev. B* **2006**, *73*, 233103.

(45) Sander, T.; Maggio, E.; Kresse, G. Beyond the Tamm-Dancoff Approximation for Extended Systems Using Exact Diagonalization. *Phys. Rev. B* **2015**, *92*, 45209.

(46) Onida, G.; Reining, L.; Rubio, A. Electronic Excitations: Density-Functional Versus Many-Body Green's-Function Approaches. *Rev. Mod. Phys.* **2002**, *74*, 601−659.

(47) Chubarov, M.; Choudhury, T. H.; Hickey, D. R.; Bachu, S.; Zhang, T.; Sebastian, A.; Bansal, A.; Zhu, H.; Trainor, N.; Das, S.; Terrones, M.; Alem, N.; Redwing, J. M. Wafer-Scale Epitaxial Growth of Unidirectional WS$_2$ Monolayers on Sapphire. *ACS Nano* **2021**, *15*, 2532−2541.

(48) Mori-Sánchez, P.; Cohen, A. J.; Yang, W. Localization and Delocalization Errors in Density Functional Theory and Implications for Band-Gap Prediction. *Phys. Rev. Lett.* **2008**, *100*, 146401.

(49) Zhao, W.; Ghorannevis, Z.; Chu, L.; Toh, M.; Kloc, C.; Tan, P.; Eda, G. Evolution of Electronic Structure in Atomically Thin Sheets of WS$_2$ and WSe$_2$. *ACS Nano* **2013**, *7*, 791−797.

(50) Schlipf, M.; Gygi, F. Optimization Algorithm for the Generation of ONCV Pseudopotentials. *Comput. Phys. Commun.* **2015**, *196*, 36−44.

(51) Qiu, D. Y.; Da Jornada, F. H.; Louie, S. G. Screening and Many-Body Effects in Two-Dimensional Crystals: Monolayer MoS$_2$. *Phys. Rev. B* **2016**, *93*, 235435.

(52) Hybertsen, M. S.; Louie, S. G. Electron Correlation in Semiconductors and Insulators: Band Gaps an Quasiparticle Energies. *Phys. Rev. B* **1986**, *34*, 5390−5415.

(53) Pizzi, G.; Vitale, V.; Arita, R.; Blugel, S.; Freimuth, F.; Geranton, G.; Gibertini, M.; Gresch, D.; Johnson, C.; Koretsune, T.; Ibanez-Azpiroz, J.; Lee, H.; Lihm, J. M.; Marchand, D.; Marrazzo, A.; Mokrousov, Y.; Mustafa, J. I.; Nohara, Y.; Nomura, Y.; Paulatto, L.; et al. Wannier90 as a Community Code: New Features and Applications. *J. Phys.: Condens. Matter* **2020**, *32*, 165902.

▢ Recommended by ACS

Extrinsic Effects on the Optical Properties of Surface Color Defects Generated in Hexagonal Boron Nitride Nanosheets

Marie Krečmarová, Juan F. Sánchez-Royo, *et al.*

SEPTEMBER 14, 2021
ACS APPLIED MATERIALS & INTERFACES   READ ☑

Enhancing Nonradiative Energy Transfer between Nitridized Carbon Quantum Dots and Monolayer WS2

Weitao Su, Yunhua Gao, *et al.*

SEPTEMBER 17, 2019
THE JOURNAL OF PHYSICAL CHEMISTRY C   READ ☑

Evolution of Nitrogen-Related Defects in Graphitic Carbon Nitride Nanosheets Probed by Positron Annihilation and Photoluminescence Spectroscopy

Biswajit Choudhury, P. K. Giri, *et al.*

APRIL 06, 2018
THE JOURNAL OF PHYSICAL CHEMISTRY C   READ ☑

Probing the Effect of Chemical Dopant Phase on Photoluminescence of Monolayer MoS2 Using in Situ Raman Microspectroscopy

Blake Birmingham, Zhenrong Zhang, *et al.*

JUNE 08, 2019
THE JOURNAL OF PHYSICAL CHEMISTRY C   READ ☑

Get More Suggestions >